PCCP

Solvent Oligomerization Pathways Facilitated by Electrolyte Additives During Solid-Electrolyte Interphase Formation

Journal:	*Physical Chemistry Chemical Physics*
Manuscript ID	CP-ART-06-2020-003286.R2
Article Type:	Paper
Date Submitted by the Author:	09-Sep-2020
Complete List of Authors:	Gibson, Luke; University of Washington, Chemical Engineering Pfaendtner, Jim; University of Washington, Chemical Engineering

Solvent Oligomerization Pathways Facilitated by Electrolyte Additives During Solid-Electrolyte Interphase Formation

Luke D. Gibson[†] and Jim Pfaendtner[*,†,‡]

[†]Department of Chemical Engineering, University of Washington, Seattle, Washington 98195
[‡]Physical Sciences Division, Pacific Northwest National Laboratory, Richland, Washington 99354

*Email: jpfaendt@uw.edu

Abstract

The solid-electrolyte interphase (SEI) layer formation is known to play an important role in determining the lifetime of lithium-ion batteries. A thin, stable SEI layer is linked to overall improved battery performance and longevity, however, the factors and mechanisms that lead to optimal SEI morphology and composition are not well understood. Inclusion of electrolyte additives (fluoroethylene carbonate, FEC; and vinylene carbonate, VC) is often necessary for improving SEI characteristics. To understand how these electrolyte additives impact SEI formation, molecular dynamics (MD) and density functional theory (DFT) simulations were employed to study the reaction networks and oligomerization pathways, respectively, for three systems containing ethylene carbonate (EC), a lithium ion, and FEC or VC. MD simulations suggest radical oligomerization pathways analogous to traditional oligomerization with nucleophilic alkoxide species via S_N1 reaction mechanisms. Both S_N1 and S_N2 mechanisms were studied for all three systems using DFT. Oligomerization reactions were studied with both a standard alkoxide species and a ring-opened EC radical as the nucleophiles and EC, FEC, and VC as the electrophiles. For all cases, FEC and VC exhibited lower free energy barriers and more stable adducts when compared with EC. We conclude that one of the roles of additives is to modify the oligomerization process of EC by introducing branching points (FEC) or termination points (VC).

1. Introduction

The need for reliable, long-term energy storage is rapidly growing, especially as renewable energy resources such as solar and wind become increasingly efficient. The lithium-ion battery (LIB) is an excellent candidate for long-term energy storage due to its high energy density; however, it suffers from irreversible capacity loss over its lifetime. There are many mechanisms that contribute to this capacity loss, such as lithium plating, dissolution of active material, separation of active material from the current collector, and solid-electrolyte interphase (SEI) formation.[1] SEI formation is considered a major contributor to overall capacity fade in LIBs and other similar battery chemistries.[1,2] Therefore, the formation of SEI and how this phenomenon proceeds in various chemical environments have remained active areas of research.[2–16]

SEI can form at both the cathode and anode interfaces likely via different mechanisms. At the cathode interface, the mechanisms that govern SEI growth is not yet fully understood. It is seen that the cathode can reduce energy barriers for ethylene carbonate (electrolyte solvent) decomposition and oligomerization in the presence of the PF_6^- anion (common Li^+ counterion).[17–19] However, the $LiPF_6$ pair is also known to decompose into LiF and the reactive PF_5 species independent of a particular electrode interface, which can give rise to PF_5-initiated reaction pathways.[19–21] At the other end of the battery at the anode interface, SEI growth is driven by reductive decomposition.[22–24] Further, at the anode side, the SEI is comprised of two zones: the inner, inorganic layer (e.g., Li_2O, LiF, Li_2CO_3) and the outer, organic layer (e.g., Li_2EDC, Li_2BDC, oligomeric species).[13,25,26] This current work is focused on understanding the mechanisms behind outer SEI growth at the anode interface wherein electron is expected to be slow. Any mention of the SEI throughout the remainder of this paper can be assumed to be referring to the anode side.

The products of these decomposition steps are believed to heavily impact the overall performance of the battery; however, it is difficult to get a clear picture of this product distribution experimentally due to the high reactivity of battery and SEI components. The models that describes how this reductive decomposition ultimately leads to the formation of the SEI layer are not fully developed and is still an ongoing area of research.[2,27] Understanding the mechanisms that drive SEI growth can grant insight into how this process can be controlled—for example, understanding how to minimize the layer thickness while still insulating the electrodes from further electrolyte decomposition.

Traditionally, a LIB is comprised of a graphitic anode, a metal oxide cathode, a separator, and an electrolyte. The electrolyte includes the Li^+ salt and the solvent. Electrolyte solvents are commonly mixtures of ethylene carbonate (EC), dimethyl carbonate (DMC), ethyl methyl carbonate (EMC), etc. with additives that are also cyclic or linear carbonate species. Popular additives are fluoroethylene carbonate (FEC) and vinylene carbonate (VC), which have been reported to increase cycling lifetime.[5] The inclusion of small weight fractions of these additives have been shown to improve a battery's performance and it is proposed that this marked improvement is due to how the additives modulate the growth mechanisms and compositions of the SEI layer.[4,14] A previous study by Delp *et al.*[28] found that the reduction potential for EC was ~0.5 V vs. Li/Li^+ (often credited for SEI formation), whereas the FEC and VC calculated reduction potentials were 0.9 and 0.8 V vs. Li/Li^+, respectively. It was also found that FEC and VC do not have high affinities for populating the Li^+ solvation shell. And although FEC and VC have higher reduction potentials, Delp *et al*. argue that high solvation shell populations are also important factors when predicting if additives are preferentially reduced over EC, thereby implying that FEC and VC may participate in SEI growth via mechanisms other than direct reduction.[28]

Experimental studies have looked at how FEC and VC affects cycling performance and how these improvements relate to the chemical structure of the SEI.[4,6,14] Wang *et al.* performed a study in which they compared the performance of FEC and VC additives in lithium-ion pouch cells.[6] They found that the inclusion of either FEC or VC yielded better coulombic efficiency, increased cycle life, smaller capacity fade, lower gas generation, and lower voltage drop during storage when compared to the control (EC:EMC, 3:7 wt% ratio). Another set of recent studies highlighted the concentration dependence of FEC on Na-battery performance (both experimentally and theoretically), in which it was found that lower concentrations of FEC led to improved SEI characteristics over higher concentrations.[29,30] Two studies by Jin *et al.* investigated the impact of FEC and VC additives on SEI composition for silicon nanowire LIBs.[4,14] They demonstrated a reduction in polyethylene oxide (PEO)-like species for FEC-containing systems when compared to EC/DMC systems using NMR techniques. Another important finding was the presence of cross-linking vinoxyl species that were generated from FEC-derived VC molecules. Furthermore, acetal carbons were shown to exist only in additive-containing systems and were attributed to the improved cross-linking of PEO polymeric species in the organic SEI. Jin *et al.* argue that the FEC additive helps to suppress the formation of soluble decomposition products by enhancing the formation of insoluble decomposition products that deposit onto the SEI, further preventing electrolyte reduction.[4,6,14]

Although experiments have provided many insights, they are limited by their lack of molecular-scale resolution, which is often required for mechanistic studies. Battery systems are particularly difficult to study experimentally due to their highly reactive components. Therefore, studying the SEI without altering the underlying chemical structures often requires cryogenic temperatures as to mitigate any unwanted side reactions upon examination.[31] Molecular

simulations can help bridge this gap by using quantum chemistry and molecular dynamics to investigate mechanisms that would otherwise be infeasible experimentally. Specifically, molecular simulations have provided great insight into the role of electrolyte additives in SEI growth. In a hybrid Monte Carlo/molecular dynamics study for sodium ion batteries, FEC was linked to improved network formation in the SEI due to its strong dipole moment, which prevented the dissolution of degradation products even in cases when FEC did not participate in any degradation reactions.[11] Another group saw a similar effect in ab initio molecular dynamics (AIMD) simulations wherein FEC decomposed to form LiF and formed connections between lithium ethylene dicarbonate (Li_2EDC) species, thereby preventing the dissolution of the commonly seen degradation product.[8] Energy landscapes for EC oligomerization via S_N1 and S_N2 reaction mechanisms have also been calculated using density functional theory (DFT). Both pathways involve an alkoxide as the nucleophile which reacts with EC to form polyethylene carbonate (PEC) via an S_N1 mechanism or PEO via an S_N2 mechanism—both species that have been detected experimentally in the outer, organic zone of the SEI.[4,14,16] In S_N1 mechanisms, the carbonyl carbon in the carbonate group (C_C) is the electrophilic site of attack, whereas in S_N2 mechanisms, the ethyl carbons (C_E) are the electrophilic sites. A diagram with the atom labels for EC and both mechanisms are depicted in Figure 1. These PEO and PEC oligomeric species have also been detected in previous experimental studies, along with several other oligomeric compounds.[4,14,32,33]

Although many studied oligomerization mechanisms involve alkoxides behaving as nucleophiles,[4,14,16,34] it is often overlooked how these alkoxides are formed. There are likely many ways in which alkoxide species can form in carbonate-based electrolytes, but the most straightforward mechanism involves the decarboxylation of a terminal carbonate group to form a terminal oxide and CO_2.[13,16]

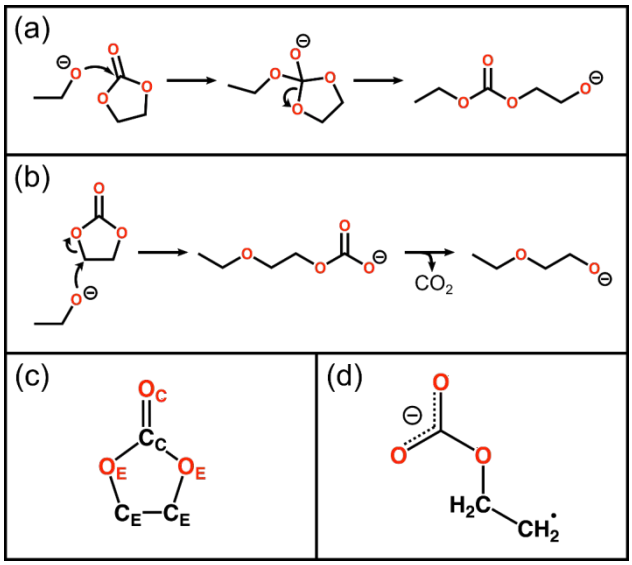

Figure 1: (a) S_N1 and (b) S_N2 mechanisms for nucleophilic attack of an EC molecule by an ethoxide. (c) EC molecule with atomic labels. "E" subscripts denote atoms are part of, or bonded to, the ethyl group and "C" subscripts denote they belong to the carbonyl group. (d) Ring-opened EC radical anion (o-EC).

Despite the current progress of simulations in understanding additive effects on SEI, there still exists a need to study these systems due to the highly complex chemical reaction networks involved in SEI growth. The role of electrolyte additives still remains unknown in the context of SEI oligomerization reactions, which is a process that has been shown to be important for EC systems.[16] To this end, we examined nucleophilic substitution pathways that include FEC and VC additives as the electrophiles, as well as ring-opened EC radical anions (o-EC, shown in Figure 1d) as a potential nucleophile. Firstly, we employed semi-empirical molecular dynamics (SEMD) simulations to explore the reaction networks of FEC or VC in the presence of EC, as well as a pure EC system as a control. For these SEMD simulations, we utilized a cost-effective Hamiltonian and enhanced sampling techniques to permit the exploration of these reaction networks. We then further verified key mechanisms that were observed with more accurate, hybrid functional DFT calculations to support our mechanistic conclusions.

Following the description of computational methods, the remainder of this paper is organized as follows. We introduce the reaction networks that were sampled and discuss key pathways that were observed. These key pathways are mechanistically verified with quantum chemistry calculations and the impact of the observed mechanisms are discussed. The paper concludes with a brief summary of our findings and their impact.

2. Methods

To gain a better insight into how FEC and VC additives affect SEI formation mechanisms, we examined three model electrolyte systems, which are listed in Table 1.

Table 1: Model Electrolyte Systems for MD

System Name	System Composition
4EC	4 EC + 1 Li^+ + 1 e^-
3EC+FEC	3 EC + 1 FEC + 1 Li^+ + 1 e^-
3EC+VC	3 EC + 1 VC + 1 Li^+ + 1 e^-

We used molecular dynamics (MD) and density functional theory (DFT) to study SEI formation with molecular-scale resolution. All MD simulations were run with the system temperature set to 300 K using the Nosé-Hoover thermostat[35,36] in the NVT ensemble and with a time step of 1 fs. To emulate 1*e* reduction, the charge and multiplicity of each system were set to 0 and doublet, respectively. The MD simulations were run using the semi-empirical PM6 level of theory[37] in the CP2K quantum chemistry MD simulation package[38–43] with the PLUMED library[44]. While PM6 has not been used to study systems of electrolytes, we have chosen it because of its high computational efficiency as a quantum chemical method that permits reactive events. A recent study from our group demonstrated that PM6 was able to reproduce the reaction network of γ-

ketohydroperoxide, a small hydrocarbon used in combustion applications.[45] Although PM6 may not quantitatively reproduce energy barriers or reaction energies for our systems, our MD simulations were aimed at exploring large reaction networks and not on recovering quantitative kinetic or thermodynamic data.

Despite the high efficiency of PM6, sufficiently sampling all of the available pathways remains an intractable problem. This is because chemical reactions are rare events that can often occur on time scales much longer than what is typically afforded to MD simulations. However, we overcome this barrier by utilizing enhanced sampling. Among many enhanced sampling methods, the metadynamics (MetaD) family of methods[46] has found frequent use for studying chemical reaction networks.[47] To this end, we have used parallel bias MetaD[48] (PBMetaD) to bias all atomic SPRINT coordinates[49], for a total of around 40 CVs in each simulation, to enhance the rate at which chemical reactions occur. The PBMetaD framework allows for simultaneous application of multiple well-tempered MetaD[50] bias potentials, in this case all one-dimensional, on different CVs within a single simulation replica. This method of using PBMetaD+SPRINT has previously been shown to be an effective tool for reaction network exploration.[45,51] The biasing parameters used in this study used a 10 kJ/mol hill height, a hill width (σ) of 0.20 for all CVs, a deposition rate of 250 ps^{-1}, and a bias factor of 150. It should be noted that in the parallel bias framework of MetaD, the hill height is divided and scaled among all CVs that are receiving bias, which merits the rather large bias factor and hill heights compared to what is found in traditional MetaD simulations. Further, in a previous study in our group, there were no significant differences in observed reaction networks when using higher vs. lower biasing rates.[45] Although the biasing rate in this study is still higher than the maximum that is used in ref. 45, our system contained five disconnected molecules or ions, thereby giving rise to a significantly increased number of CVs, which according to the

PBMetaD theory leads to a proportional decrease in the individually applied biases at any given time.

For each system in Table 1, a minimum of 50 independent MD simulations were run for ~2.5 ns each to ensure sufficient sampling of reactive pathways, following the procedure of ref. 45 in which a minimum of 45 independent MD simulations were performed due to the large phase space of SPRINT coordinates (i.e., reactive pathways). Simulations were run for ~2.5 ns because after which time, the reaction networks had converged up to secondary products (discussed in Results & Discussion). The respective simulation trajectories were analyzed using an automated reaction detection algorithm first developed in a previous study,[52] in which the molecular system is represented as a connectivity graph and treated as a hidden Markov model (HMM) to estimate the underlying connectivity by decoding the interatomic connection signals with the Viterbi algorithm. We implemented this procedure in a python package called *mdstates* to parse through trajectories and determine structures before and after reactive events, as well as compile the networks of all trajectories into a single reaction network.

All DFT calculations were performed using the quantum chemistry simulation package Gaussian 16[53] with the B3PW91 functional[54] and a 6-311++G(d,p) basis set, as well as an ultra-fine integration grid, which has been shown in literature to closely reproduce post-Hartree-Fock energies for electrolyte decomposition systems in a cost effective manner.[55,56] An implicit water solvent model was used, as implemented by the conductor polarizable continuum model[57,58] (CPCM), but with a modified dielectric constant of 89.78 to more closely match that of liquid EC.[59] Any transition states reported below were optimized to a saddle point and verified to contain only a single imaginary frequency. Further, intrinsic reaction coordinate (IRC) calculations were performed to confirm the correct reactants and products were connected by their respective

transition states. The structures for all transition states noted in this study can be found in the ESI in Table S1. Free energies reported herein were obtained via frequency calculations, which compute entropic contributions and zero-point energy corrections to enthalpy at a reference state (1 atm and 298.15 K) using the rigid rotor harmonic oscillator (RRHO) approximation.

3. Results and Discussion

In the first part of this study, we generated reaction networks for each of the systems in Table 1 using SEMD simulations with the PBMetaD+SPRINT enhanced sampling scheme described above. The reaction network, up to secondary products, for the 4EC system can be seen in Figure 2. For some of the reaction pathways, many reactions beyond secondary products were discovered but the network only shows up to secondary products given the low likelihood that tertiary and higher order products would factor as important products. The important feature present in this network is the intermediate S_N1 adduct that is highlighted in Figure 2, which connects the observed pathway to previously seen pathways in literature, namely SEI oligomerization pathways.[16] In our case, the EC molecule has an open-shell ethoxy group bonded instead of the closed-shell molecule seen in Figure 1a. This adduct forms through the attack of an intact EC molecule by a ring-opened EC radical (o-EC), as opposed to an alkoxide that is proposed in literature.[16] During this process, a CO_2 molecule is lost as the linker oxygen in the carbonate group attacks the sp^2 carbon (C_C) in the neighboring EC, suggesting that this pathway may contribute to the CO_2 evolution that is seen experimentally during SEI growth.[60] This radical mechanism facilitates the initiation of electrolyte oligomerization with only a ring-opened EC radical, which is known to be one of the first species formed during EC degradation following 1*e* reduction.[56] For the FEC- and VC-containing systems, analogous pathways were seen that

included the additives in the mechanism. The FEC and VC networks can be seen in Figures S1 and S2, respectively.

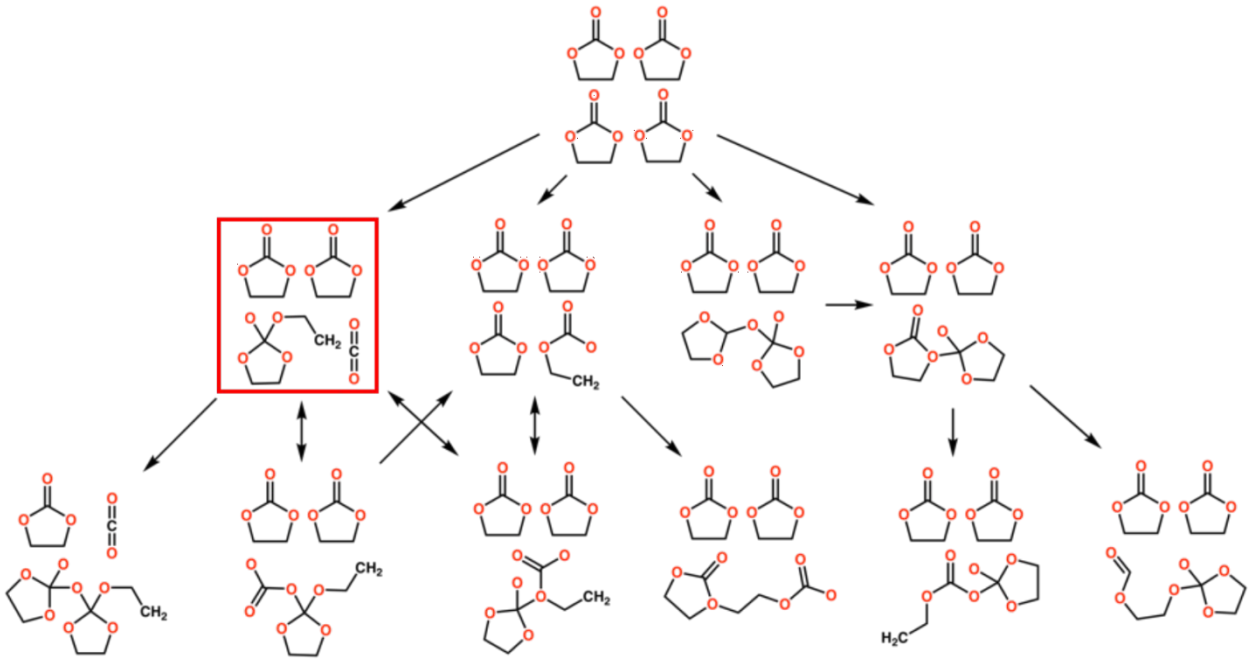

Figure 2: Reaction network of 4 EC molecules and 1 Li^+ with an extra electron. The boxed molecules indicate the node in the reaction network that contains the open-shell S_N1 adduct, as well as two intact EC molecules and CO_2. Constructed from ~50 separate reactive MD trajectories using *mdstates*. Although Li^+ was included in the simulations, it is not pictured in the reaction network.

In the following sections, we further analyze the S_N1 and S_N2 reaction mechanisms (the commonly studied oligomerization pathways) using DFT calculations to gain a more quantitative picture for these pathways with two types of nucleophiles: o-EC radical anion and ethoxide anion (the former being a novel aspect of this study and the latter being the typical nucleophile for SEI oligomerization). To further explore the use of ethoxide as a nucleophile for the studied reactions, we propose a short mechanism for its generation from two, intact EC molecules. Following this, for each nucleophilic substitution pathway, we examine how the presence of electrolyte additives (FEC and VC) impact the energetics of each reaction as compared to EC. And lastly, we connect

some predicted additive oligomerization products in this study to cross-linking groups that have been experimentally linked to improved battery performance.[4,14]

Proposed Alkoxide Formation Mechanism

Although the observed reaction in the reaction network involved an o-EC radical, we also consider the analogous mechanisms with an ethoxide anion for comparison, which has previously been studied in the case of ethoxide-EC oligomerization.[16]

As mentioned previously, there are many potential mechanisms through which alkoxides can form as a result of electrolyte decomposition, although they are seldom discussed in literature. Herein, we propose a simple mechanism in which two o-EC radical anions react via hydrogen transfer to ultimately form ethoxide + CO_2 or ethenolate + CO_2, shown in Figure 3. The adduct formed after the hydrogen transfer is significantly more stable than the two o-EC radical anions, which is not surprising due to the reconciliation of the two radicals to form closed-shell structures. Computing the energy barrier separating these two states, however, is non-trivial and would require non-adiabatic calculations of the coupling between the singlet and triplet states along the reaction coordinate. This is beyond the scope of this study, but it provides an interesting point for further investigation. The formation of the two alkoxides are uphill in enthalpy, but the formation of the ethenolate exhibits a net decrease in free energy. The ethenolate species differs from ethoxide in two ways: 1) the formation of ethenolate passes through a transition state (denoted by the double dagger, ‡, in Figure 3), and 2) the molecular structure is resonance stabilized, allowing the negative charge to delocalize across the molecule. This resonance stabilization, however, discourages the ethenolate species from reacting any further via the nucleophilic substitution mechanisms discussed herein. The ethoxide formation process, on the other hand, does not pass

through a transition state on the potential energy surface (i.e., no saddle point with a single imaginary frequency) and maintains the charge localization on the oxygen.

This hypothesized hydrogen transfer reaction is only one of many possible reactions that can occur between two o-EC radicals. Commonly seen structures that can stem from the reaction of two o-EC radicals are lithium ethylene dicarbonate (Li_2EDC) and lithium butylene dicarbonate (Li_2BDC).[59,61–63] For comparison, using the same reference and level of theory as in Figure 3, the free energies of reaction to form $Li_2EDC + C_2H_4$ or Li_2BDC from two o-EC radicals are -60.6 and -71.4 kcal/mol, respectively. This result demonstrates that the proposed H-transfer reaction step shares a similar free energy of reaction; however, we note that it is important to understand both the kinetic and thermodynamic aspects of a reaction to provide quantitative comparisons. Our result simply demonstrates that the driving force for the H-transfer reaction step is comparable to that of Li_2EDC or Li_2BDC formation and will be further investigated in a future study.

This proposed mechanism for ethoxide formation is not necessarily expected to have a high rate of reaction in a battery due to the dependence on two o-EC radicals finding each other. However, this reaction can be thought of as an initiation reaction prior to oligomerization via the S_N1 and S_N2 mechanisms and thus does not require a high rate of reaction.

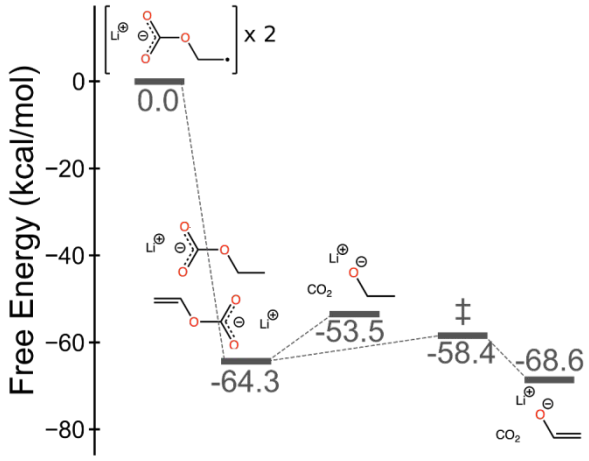

Figure 3: Free energy diagram of ethoxide and ethenolate generation via hydrogen abstraction between two o-EC radicals. Reaction progress is shown along the x-axis. A single transition state is denoted by the double dagger (‡).

S_N1 Oligomerization Mechanism

Free energy diagrams for the S_N1 oligomerization mechanism can be seen in Figure 4. Two mechanisms are considered in which either an ethoxide (Figure 4a) or o-EC radical (Figure 4b) act as the nucleophile. In both cases, EC, FEC, and VC are considered as electrophiles. Each state in Figure 4 (and Figure 5) is arbitrarily labeled according to the electrophile of the pathway and the order of appearance (e.g., EC-1 is the first structure in the mechanism with EC as the electrophile). Below each free energy diagram, the corresponding mechanism for FEC is shown. The EC and VC mechanisms are analogous and can be found in Figure S3.

The ethoxide mechanism in Figure 4a is comprised of two reactions. The first step involves a change in configuration (not depicted) and attack of the ethoxide on the C_C of the electrophile. The reactive step of the ethoxide attacking the electrophile for each of the three pathways was a barrierless reaction and did not exhibit a transition state. Similarly, a transition state could not be located for the ring-opening reaction (second step) in the mechanism.

The EC pathway in the ethoxide mechanism (Figure 4a) exhibits relatively small changes in free energy (±1 kcal/mol). From the FEC and VC pathways, it is clear that the presence of a fluorine atom or double bond impacts the energy landscape for both the ethoxide and radical S_N1 mechanisms. We see for all reaction steps FEC and VC exhibit drops in energy, with FEC consistently ~3 kcal/mol lower in free energy than VC throughout the mechanisms. It is not expected that VC will continue to react via the same S_N1 mechanism with another EC because the final structure, VC-3, will sacrifice resonance stability of the oxide anion, as seen previously with the ethenolate species in Figure 3. The energetics behind further oligomerization from the VC-3

structure can be seen in Figure S4, in which both S_N1 and S_N2 oligomerization mechanisms yield positive free energies of reaction (relative to VC-3 as reference) when reacting with EC. This result implies that VC may act as a terminator for oligomerization if further reactions are unfavorable. In contrast to VC-3, FEC-3 is only metastable and the fluorine atom can be easily abstracted by a lithium ion to form an aldehyde. This aldehyde is susceptible to further reactions with nucleophiles and is discussed later in the paper.

While the ethoxide S_N1 mechanisms consistently exhibit negative free energies, the radical S_N1 mechanisms (Figure 4b) are higher in energy. The reaction mechanism is analogous to the one in Figure 4a, but with a concerted loss of CO_2 as the nucleophilic oxygen attacks the C_C, which does exhibit a transition state. The first reaction has a large free energy barrier of approximately 30 kcal/mol. In this step, the linker O_E oxygen in the radical attacks the C_C in the neutral molecule, thereby shedding a CO_2 molecule from the o-EC radical. The FEC and VC radical pathways slightly diminish the reaction free energy barrier (FEC-5 and VC-5) and have lower free energies for the adducts FEC-6 and VC-6 when compared to EC-6. The last step in the mechanism, a ring-opening reaction, yields products that are overall net decreases in free energy for the FEC and VC pathways, whereas the EC pathway ends with a net increase in free energy. However, as before, the VC species are not expected to react any further.

The energetic landscape seen in Figure 4 suggests that nucleophilic alkoxides and radicals will preferentially attack FEC and VC over another EC. Particularly in the case of the radical S_N1 mechanism, the presence of an FEC or VC will shift the chemical equilibrium towards products (VC-7 and FEC-7) due to their negative free energies of reaction, as opposed to the unfavorable radical EC S_N1 pathway. These additive products are even further favored due to faster kinetics that result from a diminished energy barrier when compared to EC. Further, the reverse reactions

for the FEC and VC pathways have increased free energy barriers relative to EC pathways, which reinforces the claim that FEC and VC preferentially react in the kinetically controlled SEI growth process.

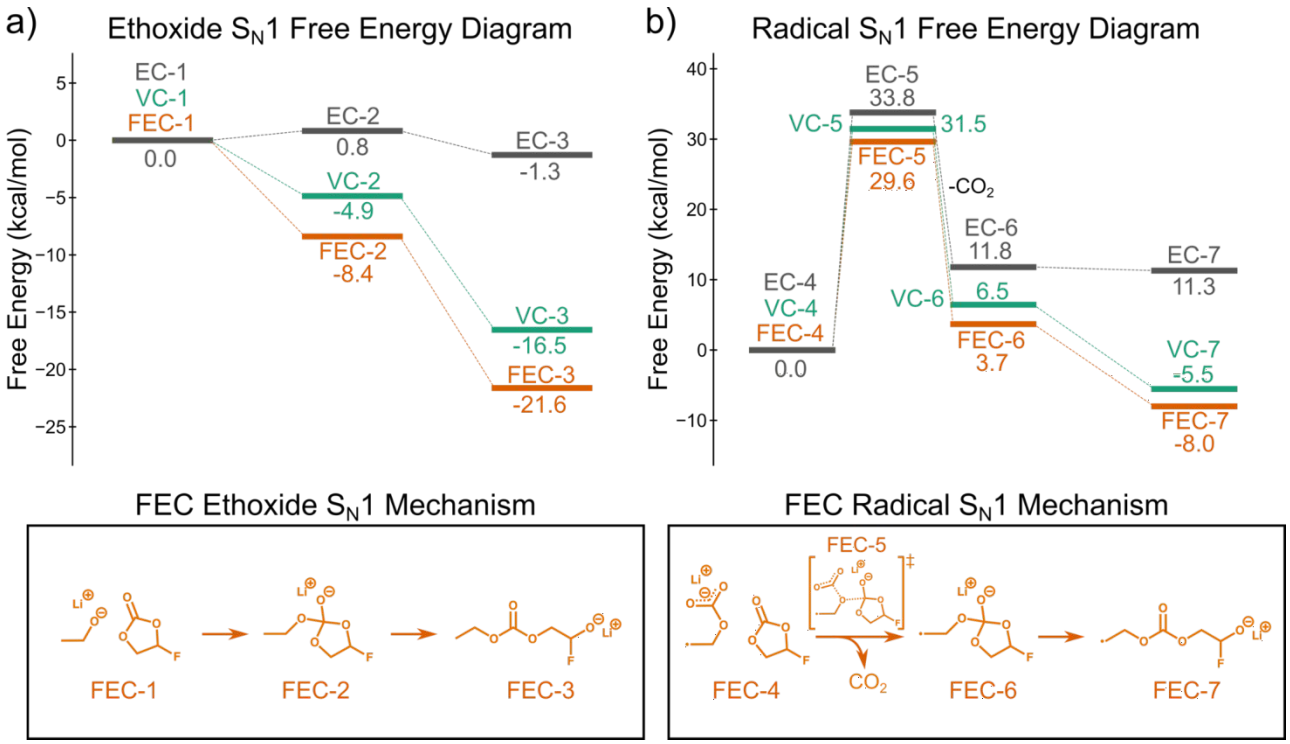

Figure 4: Free energy diagrams and mechanisms for a single step of S_N1 oligomerization in which an ethoxide (a) or radical o-EC (b) acts as the nucleophile. The gray pathway denotes that EC is being attacked, green is VC, and orange is FEC. Mechanisms shown below each diagram only depict the FEC case. Analogous mechanisms are seen for EC and VC systems and can be found in the Electronic Supplementary Information in Figure S3. Radical locations are denoted with a dot (•) in the radical mechanism in (b). EC-5, FEC-5, and VC-5 correspond to the transition states in the first reactive step.

S_N2 Oligomerization Mechanism

The S_N2 oligomerization mechanism was also investigated because it produces PEO chains, which have been detected in the SEI,[4,14] and can occur with the same reactants. In this mechanism, following a reconfiguration of the fully relaxed structure (not depicted), the nucleophilic oxygen attacks a C_E atom and breaks the opposite C_E-O_E bond in a concerted motion, as shown in Figure 1b. The second and final step regenerates the nucleophilic oxygen through a

decarboxylation reaction with no transition state. This mechanism was only studied for EC and FEC (Figure 5) and not VC because there are no aliphatic C_E carbons available for nucleophilic attack in VC. The free energy diagram and mechanisms are shown in Figure 5. As before, the EC mechanisms can be found in the Electronic Supplementary Information in Figure S5.

The initial free energy barrier for ethoxide attacking a C_E carbon on EC was calculated to be 16.8 kcal/mol followed by a large, net drop in free energy to -24.9 kcal/mol. The large drop in energy is consistent with what was seen in ref. 16, but the initial energy barrier is approximately half of what was previously reported. This discrepancy is due to the different solvent models used (CPCM in this study, SMD in ref. 16). The SMD implicit solvent model consistently reports lower energies for the initial structures of each mechanism and thus increases all other energies relative to the starting point. The last step of the mechanism in which the nucleophilic oxygen is regenerated via decarboxylation was calculated to be entirely uphill in free energy, but still exhibits an overall drop in free energy to -15.6 kcal/mol relative to EC-8.

Compared to the EC pathway, the initial free energy barrier (FEC-9) and first adduct (FEC-10) for FEC were calculated to be lower by approximately 4 kcal/mol. However, instead of the decarboxylation step imparting an increase in free energy, FEC-11 exhibited an even further drop in free energy to -35.3 kcal/mol. This final structure is approximately 20 kcal/mol more stable than EC-11 and the barrier and adduct are also lower in free energy, implying a greater propensity for an ethoxide to attack an FEC molecule over another EC. As before with FEC, the bonded fluorine is only metastable and is readily abstracted by neighboring Li^+ or H^+ forming a reactive aldehyde. Due to the chiral center of FEC, there are multiple pathways to produce isomers for the species in Figures 4 and 5, but we have only reported the lowest energy pathway.

The radical S_N2 free energy diagram in Figure 5b exhibits a similar pattern as with Figure 5a, but with a different energy scale on the y-axis. The final free energy for the ethoxide (EC-11, -15.6 kcal/mol) and radical (EC-15, -4.6 kcal/mol) mechanisms are net negative, which imply that both mechanisms are favored with chemical equilibria shifted towards these oligomer products. In the case of EC-11, this matches the finding that PEO-like oligomers are detected in SEI. Interestingly, after the first radical oligomerization step, the EC-15 carries a terminal oxide that can now act as the nucleophile in the mechanism and can proceed through lower energy barrier propagation reactions, similar to the barrier shown in Figure 5a. This suggests that the radical S_N2 reaction with an intact EC is possible and may also contribute to the concentration of PEO-like oligomers detected experimentally in the SEI.

Both FEC-11 and FEC-15 become more stable after decarboxylation, implying that the equilibrium is shifted towards the products of nucleophilic attack of FEC molecules. The S_N2 FEC pathways are also kinetically favored due to their diminished energy barriers for the forward reactions and increased energy barrier for the reverse reactions.

As with the S_N1 oligomerization mechanisms, the final products from the FEC pathways in Figure 5 can easily have their fluorine atoms abstracted, leading to the formation of an aldehyde. This aldehyde formation from FEC species can further lead to acetal carbon formation, an interesting aspect that is discussed next.

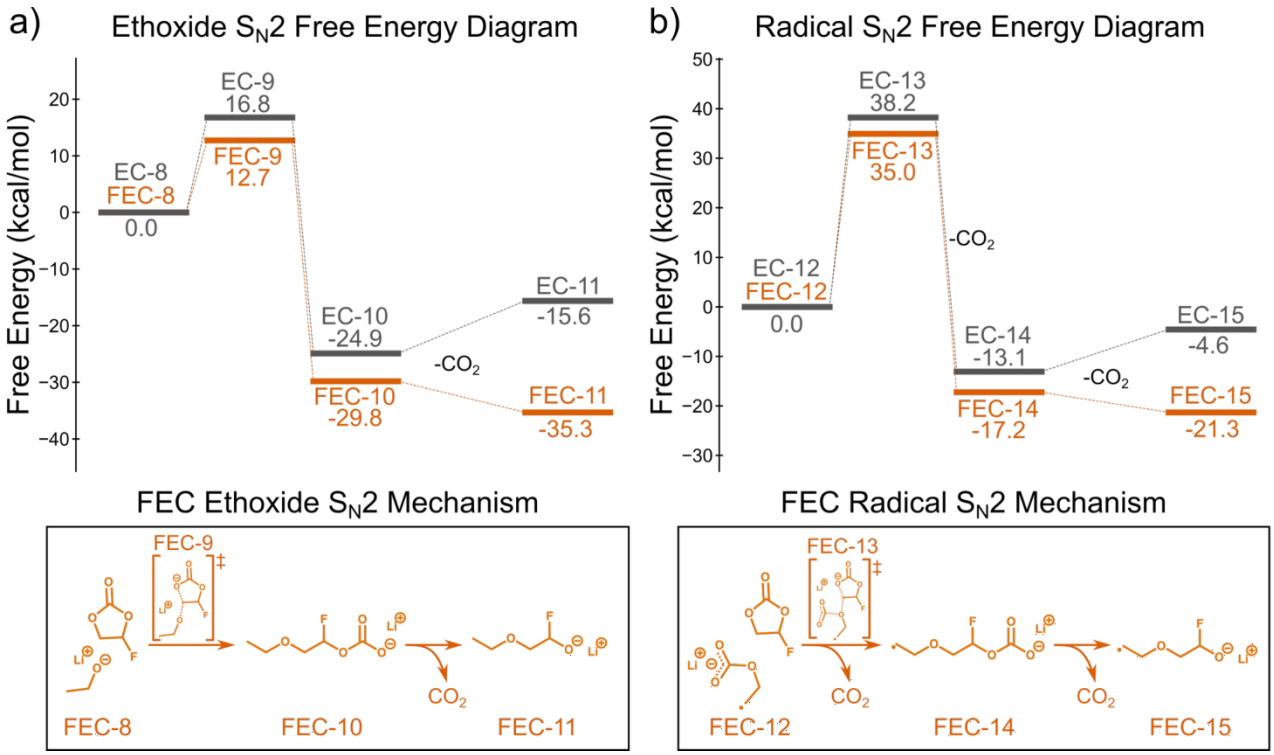

Figure 5: Free energy diagrams and mechanisms for a single step of S_N2 oligomerization in which an ethoxide (a) or radical o-EC (b) acts as the nucleophile. The gray pathway denotes that EC is the electrophile in the mechanism and orange is FEC. Mechanisms shown below each diagram only depict the FEC case. Analogous mechanisms are seen for the EC system and can be found in the Electronic Supplementary Information in Figure S5. Radical locations are denoted with a dot (•) in the radical mechanism in (b). EC-9, FEC-9, EC-13, and FEC-13 correspond to the transition states in the first reactive step.

Acetal Carbon Formation

Acetal carbons act as crosslinkers in the oligomeric SEI and can potentially account for the marked improvement in performance for batteries containing FEC in the electrolyte, especially in battery chemistries that suffer from large volume changes during cycling.[4,9,12–14]

As mentioned previously, the final products in each FEC mechanism can have the fluorine atom abstracted by a lithium ion to form an aldehyde in a barrierless, single step process, shown in Figure 6. This reaction produces LiF and a neutral aldehyde, denoted by an asterisk (*) following the name of the parent molecule from which it reacted.

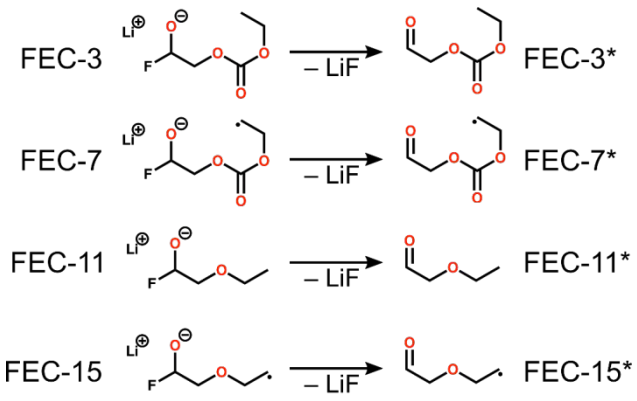

Figure 6: Mechanism for aldehyde formation for each of the terminal species in the FEC pathways. The species names along the right are simply the original molecule's name followed by an asterisk (*) to denote the aldehyde form.

This aldehyde group is highly reactive with nucleophiles. With the aldehydes as the starting points (FEC-3*, FEC-7*, FEC-11*, FEC-15*), we have calculated the free energy and enthalpy of reaction for acetal carbon formation via nucleophilic attack with an ethoxide, which can be seen in Figure 7. The general reaction scheme is seen in the upper right corner of Figure 7, with the green X representing the different moieties from each of the four mechanisms. Each reaction was found to be barrierless and thus no transition state is reported. Each moiety is labeled with the corresponding reaction energies on the bar plot.

While the enthalpy of reaction for each of the reactions was negative, all free energies of reaction were positive. The free energies of reaction were approximately +17 kcal/mol more than the enthalpy of reaction across the board, implying that the entropic losses for this type of reaction are large at 300 K.

As a result, the S_N1-derived species are not expected to undergo this acetal formation reaction due to the largely positive free energies of reaction, whereas the S_N2-derived species are far more likely with free energies of reaction very close to zero. Further, the S_N2-derived species

have negative enthalpies of reaction, which implies that a stable product will be formed if the reaction does occur.

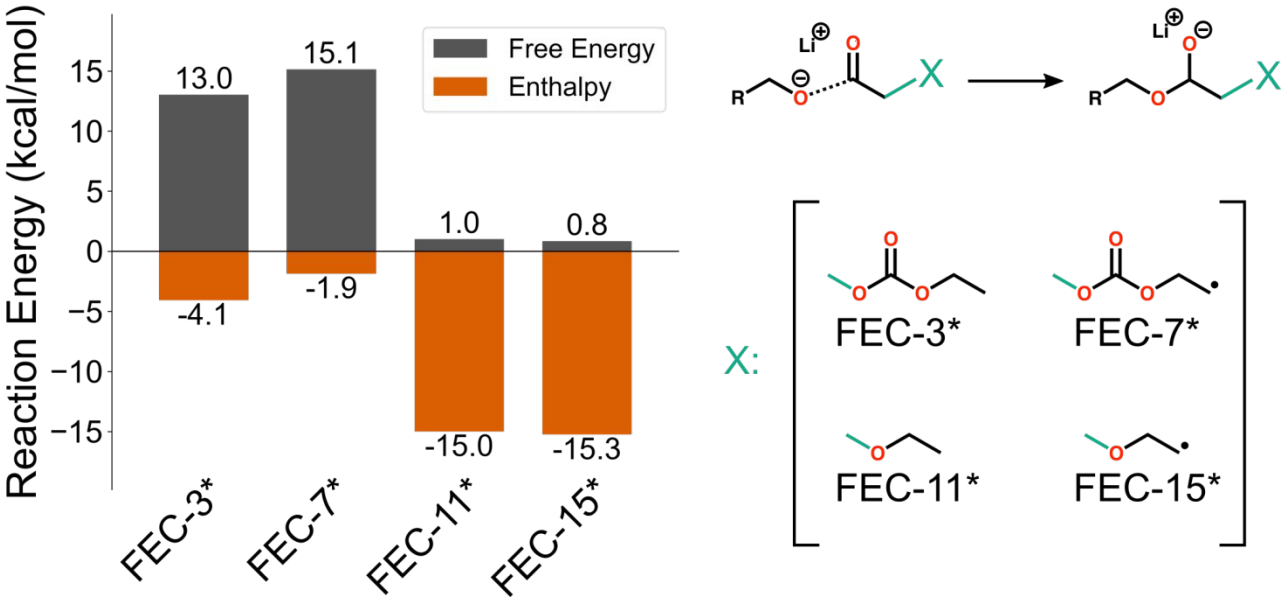

Figure 7: Reaction energies (enthalpy and free energy) for the nucleophilic attack of an aldehyde by an alkoxide, shown in the upper-right, where X corresponds to each of the four labeled groups. The green bond in each of the groups can be considered the same bond in the shown reaction. The labels on the groups correspond to the reaction energies in the left plot. Radical locations are denoted with a dot (•) in FEC-7* and FEC-15*.

4. Conclusions

In this study, we have examined how electrolyte additives FEC and VC impact the energetics of oligomerization reactions and compared to the case of EC oligomerization. We analyzed S_N1 and S_N2 oligomerization mechanisms in which two possible nucleophiles attack either an EC, FEC, or VC. The two nucleophiles studied were an ethoxide anion (for which we proposed a formation mechanism) and the o-EC radical anion. We find in all cases that FEC and VC mechanisms exhibit lower energy barriers and more stable adducts as compared to the analogous EC mechanisms. Moreover, we have shown the feasibility of these mechanisms with the o-EC radical anion acting as the nucleophile, in which CO_2 formation is seen in the first step

of each mechanism, a product that is seen in experiment. Despite the large body of work that has studied these electrolyte additives, the mechanisms by which they improve battery performance are still not well understood. This study elucidates some of the potential roles of FEC and VC as electrolyte additives.

Matching previous studies,[4,14,16,34] we predict EC oligomerization via both the S_N1 and S_N2 mechanisms with the former being kinetically favorable and the latter being thermodynamically favorable. Given our results, we conclude that the presence of electrolyte additives works to modulate this oligomerization process by either introducing branching points (FEC) or termination points (VC). The branching points generated by FEC are formed via S_N2 reaction of an FEC additive with a nucleophile to ultimately form an aldehyde terminal group and LiF salt. This aldehyde group can behave as an electrophile that is susceptible to reaction with another nucleophile (e.g., another oligomer). In this process, an acetal carbon is formed, which allows for further oligomerization via the newly formed oxide group. These branching points generated from FEC provide sites for cross-linking in the oligomeric SEI, which would reduce oligomer solubility in the liquid electrolyte. VC, on the other hand, can only undergo S_N1 reactions, which form a resonance stabilized oxide group that slows further oligomerization, thereby rendering reactions with VC an effective termination step.

Furthermore, the proposed roles of these additives during oligomerization do not necessitate high concentrations of either FEC or VC and may explain why small quantities of either additive provide improved SEI characteristics. Lastly, the proposed radical pathways also only require 1*e* reduction and, depending on the availability of reducing electrons and distance from the anode, a second reduction reaction may be significantly slower and thus would favor the proposed mechanisms.

Conflicts of Interest

There are no conflicts to declare.

Acknowledgements

This research was entirely supported by the U.S. Department of Energy, Office of Science, Basic Energy Sciences, CPIMS Program, under Award DE-SC0019483. LDG acknowledges the National Science Foundation traineeship DGE-1633216. Part of the simulations in this work was facilitated though the use of advanced computational, storage, and networking infrastructure provided by the Hyak supercomputer system and funded by the STF at the University of Washington. The authors would like to thank Dr. Chowdhury Ashraf for his careful reading of this manuscript and helpful discussions and Dr. Christopher Mundy for helpful conversations.

Electronic Supplementary Information

Additional information includes reaction networks and reaction mechanisms that were omitted from the main text. Structures for all transition states noted in this work are also included.

References

1 P. Arora, R. E. White and M. Doyle, *J. Electrochem. Soc.*, 1998, **145**, 3647–3667.
2 K. Ushirogata, K. Sodeyama, Z. Futera, Y. Tateyama and Y. Okuno, *J. Electrochem. Soc.*, 2015, **162**, A2670–A2678.
3 K. U. Schwenke, S. Solchenbach, J. Demeaux, B. L. Lucht and H. A. Gasteiger, *J. Electrochem. Soc.*, 2019, **166**, A2035–A2047.
4 Y. Jin, N. J. H. Kneusels, P. C. M. M. Magusin, G. Kim, E. Castillo-Martínez, L. E. Marbella, R. N. Kerber, D. J. Howe, S. Paul, T. Liu and C. P. Grey, *J. Am. Chem. Soc.*, 2017, **139**, 14992–15004.
5 K. Ushirogata, K. Sodeyama, Y. Okuno and Y. Tateyama, *J. Am. Chem. Soc.*, 2013, **135**, 11967–11974.
6 D. Y. Wang, N. N. Sinha, J. C. Burns, C. P. Aiken, R. Petibon and J. R. Dahn, *J. Electrochem. Soc.*, 2014, **161**, A467–A472.
7 H. Kumar, E. Detsi, D. P. Abraham and V. B. Shenoy, *Chem. Mater.*, 2016, **28**, 8930–8941.
8 Y. Okuno, K. Ushirogata, K. Sodeyama and Y. Tateyama, *Phys. Chem. Chem. Phys.*, 2016, **18**, 8643–8653.
9 Q. Li, X. Liu, X. Han, Y. Xiang, G. Zhong, J. Wang, B. Zheng, J. Zhou and Y. Yang, *ACS Appl. Mater. Interfaces*, 2019, **11**, 14066–14075.
10 K. Leung and J. Budzien, *Phys. Chem. Chem. Phys.*, 2010, **12**, 6583–6586.

11 N. Takenaka, H. Sakai, Y. Suzuki, P. Uppula and M. Nagaoka, *J. Phys. Chem. C*, 2015, **119**, 18046–18055.
12 K. Leung, S. B. Rempe, M. E. Foster, Y. Ma, J. M. Martinez del la Hoz, N. Sai and P. B. Balbuena, *J. Electrochem. Soc.*, 2014, **161**, A213–A221.
13 I. A. Shkrob, J. F. Wishart and D. P. Abraham, *J. Phys. Chem. C*, 2015, **119**, 14954–14964.
14 Y. Jin, N. J. H. Kneusels, L. E. Marbella, E. Castillo-Martínez, P. C. M. M. Magusin, R. S. Weatherup, E. Jónsson, T. Liu, S. Paul and C. P. Grey, *J. Am. Chem. Soc.*, 2018, **140**, 9854–9867.
15 Y. Wang and P. B. Balbuena, *J. Phys. Chem. B*, 2002, **106**, 4486–4495.
16 S. E. Burkhardt, *J. Electrochem. Soc.*, 2017, **164**, A684–A690.
17 S. Xu, G. Luo, R. Jacobs, S. Fang, M. K. Mahanthappa, R. J. Hamers and D. Morgan, *ACS Appl. Mater. Interfaces*, 2017, **9**, 20545–20553.
18 S. A. Needham, G. X. Wang, H. K. Liu, V. A. Drozd and R. S. Liu, *J. Power Sources*, 2007, **174**, 828–831.
19 J. L. Tebbe, T. F. Fuerst and C. B. Musgrave, *ACS Appl. Mater. Interfaces*, 2016, **8**, 26664–26674.
20 S. E. Sloop, J. K. Pugh, S. Wang, J. B. Kerr and K. Kinoshita, *Electrochem. Solid-State Lett.*, 2001, **4**, A42.
21 K. Tasaki, K. Kanda, S. Nakamura and M. Ue, *J. Electrochem. Soc.*, 2003, **150**, A1628.
22 E. Peled, *J. Electrochem. Soc.*, 1979, **126**, 2047.
23 D. Aurbach, *J. Power Sources*, 2000, **89**, 206–218.
24 D. Aurbach, B. Markovsky, A. Shechter and Y. Ein-Eli, *J. Electrochem. Soc.*, 1996, **143**, 3809–3820.
25 A. Wang, S. Kadam, H. Li, S. Shi and Y. Qi, *NPJ Comput. Mater.*, , DOI:10.1038/s41524-018-0064-0.
26 Y. Li, K. Leung and Y. Qi, *Acc. Chem. Res.*, 2016, **49**, 2363–2370.
27 M. Nie, D. Chalasani, D. P. Abraham, Y. Chen, A. Bose and B. L. Lucht, *J. Phys. Chem. C*, 2013, **117**, 1257–1267.
28 S. A. Delp, O. Borodin, M. Olguin, C. G. Eisner, J. L. Allen and T. R. Jow, *Electrochim. Acta*, 2016, **209**, 498–510.
29 M. Dahbi, T. Nakano, N. Yabuuchi, S. Fujimura, K. Chihara, K. Kubota, J. Y. Son, Y. T. Cui, H. Oji and S. Komaba, *ChemElectroChem*, 2016, **3**, 1856–1867.
30 A. Bouibes, N. Takenaka, T. Fujie, K. Kubota, S. Komaba and M. Nagaoka, *ACS Appl. Mater. Interfaces*, 2018, **10**, 28525–28532.
31 Y. Li, Y. Li, A. Pei, K. Yan, Y. Sun, C. L. Wu, L. M. Joubert, R. Chin, A. L. Koh, Y. Yu, J. Perrino, B. Butz, S. Chu and Y. Cui, *Science (80-.).*, 2017, **358**, 506–510.
32 J. Henschel, C. Peschel, F. Günter, G. Reinhart, M. Winter and S. Nowak, *Chem. Mater.*, 2019, **31**, 9977–9983.
33 R. Sahore, F. Dogan and I. D. Bloom, *Chem. Mater.*, 2019, **31**, 2884–2891.
34 I. A. Shkrob, Y. Zhu, T. W. Marin and D. Abraham, *J. Phys. Chem. C*, 2013, **117**, 19270–19279.
35 S. Nosé, *J. Chem. Phys.*, 1984, **81**, 511–519.
36 S. Nosé, *Mol. Phys.*, 2002, **100**, 191–198.
37 J. J. P. Stewart, *J. Mol. Model.*, 2007, **13**, 1173–1213.
38 J. VandeVondele and J. Hutter, *J. Chem. Phys.*, 2003, **118**, 4365–4369.
39 J. Hutter, M. Iannuzzi, F. Schiffmann and J. VandeVondele, *Wiley Interdiscip. Rev.*

Comput. Mol. Sci., 2014, **4**, 15–25.
40 J. Kolafa, *J. Comput. Chem.*, 2004, **25**, 335–342.
41 O. Schütt, P. Messmer, J. Hutter and J. VandeVondele, in *Electronic Structure Calculations on Graphics Processing Units: From Quantum Chemistry to Condensed Matter Physics*, John Wiley & Sons, Ltd, Chichester, UK, 2016, pp. 173–190.
42 U. Borštnik, J. Vandevondele, V. Weber and J. Hutter, *Parallel Comput.*, 2014, **40**, 47–58.
43 M. Frigo and S. G. Johnson, in *Proceedings of the IEEE*, 2005, vol. 93, pp. 216–231.
44 G. A. Tribello, M. Bonomi, D. Branduardi, C. Camilloni and G. Bussi, *Comput. Phys. Commun.*, 2014, **185**, 604–613.
45 C. D. Fu and J. Pfaendtner, *J. Chem. Theory Comput.*, 2018, **14**, 2516–2525.
46 O. Valsson, P. Tiwary and M. Parrinello, *Annu. Rev. Phys. Chem.*, 2016, **67**, 159–184.
47 S. Zheng and J. Pfaendtner, *Mol. Simul.*, 2015, **41**, 55–72.
48 J. Pfaendtner and M. Bonomi, *J. Chem. Theory Comput.*, 2015, **11**, 5062–5067.
49 F. Pietrucci and W. Andreoni, *Phys. Rev. Lett.*, 2011, **107**, 1–4.
50 A. Barducci, G. Bussi and M. Parrinello, *Phys. Rev. Lett.*, 2008, **100**, 1–4.
51 S. Zheng and J. Pfaendtner, *J. Phys. Chem. C*, 2014, **118**, 10764–10770.
52 L. P. Wang, R. T. McGibbon, V. S. Pande and T. J. Martinez, *J. Chem. Theory Comput.*, 2016, **12**, 638–649.
53 M. J. Frisch, G. W. Trucks, H. B. Schlegel, G. E. Scuseria, M. A. Robb, J. R. Cheeseman, G. Scalmani, V. Barone, G. A. Petersson, H. Nakatsuji, X. Li, M. Caricato, A. V. Marenich, J. Bloino, B. G. Janesko, R. Gomperts, B. Mennucci, H. P. Hratchian, J. V. Ortiz, A. F. Izmaylov, J. L. Sonnenberg, D. Williams-Young, F. Ding, F. Lipparini, F. Egidi, J. Goings, B. Peng, A. Petrone, T. Henderson, D. Ranasinghe, V. G. Zakrzewski, J. Gao, N. Rega, G. Zheng, W. Liang, M. Hada, M. Ehara, K. Toyota, R. Fukuda, J. Hasegawa, M. Ishida, T. Nakajima, Y. Honda, O. Kitao, H. Nakai, T. Vreven, K. Throssell, J. Montgomery, J. A., J. E. Peralta, F. Ogliaro, M. J. Bearpark, J. J. Heyd, E. N. Brothers, K. N. Kudin, V. N. Staroverov, T. A. Keith, R. Kobayashi, J. Normand, K. Raghavachari, A. P. Rendell, J. C. Burant, S. S. Iyengar, J. Tomasi, M. Cossi, J. M. Millam, M. Klene, C. Adamo, R. Cammi, J. W. Ochterski, R. L. Martin, K. Morokuma, O. Farkas, J. B. Foresman and D. J. Fox, *Gaussian 16, Revision A.03*, Gaussian, Inc., Wallingford, CT, 2016.
54 A. D. Becke, *J. Chem. Phys.*, 1993, **98**, 5648–5652.
55 Y. K. Han and S. U. Lee, *Theor. Chem. Acc.*, 2004, **112**, 106–112.
56 Y. Wang, S. Nakamura, M. Ue and P. B. Balbuena, *J. Am. Chem. Soc.*, 2001, **123**, 11708–11718.
57 V. Barone and M. Cossi, *J. Phys. Chem. A*, 1998, **102**, 1995–2001.
58 M. Cossi, N. Rega, G. Scalmani and V. Barone, *J. Comput. Chem.*, 2003, **24**, 669–681.
59 K. Tasaki, *J. Phys. Chem. B*, 2005, **109**, 2920–2933.
60 M. Onuki, S. Kinoshita, Y. Sakata, M. Yanagidate, Y. Otake, M. Ue and M. Deguchi, *J. Electrochem. Soc.*, 2008, **155**, A794–A797.
61 S. P. Kim, A. C. T. Van Duin and V. B. Shenoy, *J. Power Sources*, 2011, **196**, 8590–8597.
62 M. J. Boyer and G. S. Hwang, *Electrochim. Acta*, 2018, **266**, 326–331.
63 O. Borodin, G. D. Smith and P. Fan, *J. Phys. Chem. B*, 2006, **110**, 22773–22779.